

Label-free microendoscopy using a micro-needle imaging probe for *in vivo* deep tissue imaging

KWANJUN PARK,¹ JUNE HOAN KIM,² TAEDONG KONG,¹ WOONG SUN,² JONGHWAN LEE,³ TAESEOK DANIEL YANG,^{3,4,5}  AND YOUNGWOON CHOI^{1,4,6} 

¹Department of Bioengineering, Korea University, Seoul 02841, South Korea

²Department of Anatomy, College of Medicine, Korea University, Seoul 02841, South Korea

³School of Biomedical Engineering, Brown University, Providence, Rhode Island 02912, USA

⁴School of Biomedical Engineering, Korea University, Seoul 02841, South Korea

⁵danielyang77@gmail.com

⁶youngwoon@korea.ac.kr

Abstract: We report a label-free imaging method for microendoscopy that uses a needle-type imaging probe. We inserted a thin GRIN lens that had been attached to a fiber bundle into a medical-grade needle that was used as an imaging probe. The introduction of the needle probe into biological tissue allows for direct access to deep regions that we otherwise could not achieve because of the multiple light scattering. To minimize invasiveness, we introduced the illuminating probe on the tissue surface, using an oblique back-illumination configuration. We achieved three-dimensional depth imaging by changing the depth of penetration. Since only the imaging probe goes deep into the tissue while leaving the illumination channels outside, the achievable signal depends on the location of the illumination channels. We explored this point and investigated the optimal condition for the illumination distance in a systematic way. We also applied this method to *ex vivo*, as well as *in vivo*, imaging of a mouse brain, and confirmed that we had visualized the microvasculature embedded deep within the brain.

© 2020 Optical Society of America under the terms of the [OSA Open Access Publishing Agreement](#)

1. Introduction

In the past decades, advances in optical microscopic techniques have made possible three-dimensional (3-D) imaging of biological tissue. This plays an important role in diverse research areas, ranging from basic science to medicine [1]. Optical imaging modalities, such as confocal and multiphoton microscopy, are often used in these research areas, providing superior high-resolution 3-D images [2–13]. However, the penetration depth for these imaging modalities is limited to a few hundred micrometers at most due to the multiple light scattering caused by biological tissue [14]. Recently, adaptive optics (AO) techniques, based on sensitive wavefront detection and control apparatus, have shown some meaningful signs of progress in overcoming these imaging depth restrictions. Thus, they have been able to demonstrate high-resolution and high-contrast imaging of biological samples [14–19]. Even with these technical achievements, limitation of penetration depth is still inevitable, especially in the deeper regions, because of strong multiple scattering of light within biological tissue.

Lately, an imaging method called oblique back-illumination microscopy (OBM) has been introduced. This method is capable of acquiring wide-field phase-gradient images of thick tissues [20–27]. The image generation mechanism in the OBM method was numerically [20] and theoretically [28,29] explored. Although OBM's optical configuration relies on reflection geometry, it generates the image based on the two oblique light transmissions through the sample from the backside. Those result in phase-gradient information for the sample structure and

thus produce superior contrast for purely phase objects. Since multiple scattering disrupts the propagation of light within the biological tissue, epi-illumination that is introduced from the outside can reach the sample's backside via the diffusion process. This allows illumination that is transmitted through the sample to arrive at the detector. By using this unique illumination, OBM can generate high-contrast transmission images at the target depth. In addition, employing two different illumination channels leads to the capability of phase-gradient imaging. Since the OBM contrast is generated by the obliqueness difference of the two light paths, the numerical aperture (NA) of the imaging lens enough for accepting the light is essential to form the OBM contrast. The light reaches the detector at a certain angle because of the illumination configuration where light comes from the side. By acquiring two images at two illuminations, a differential image can be generated by appropriate image processing.

Because this method is based on the diffusion process to deliver light, its multiple scattering does not affect the image formation in OBM configurations. However, the achievable imaging depth of OBM is still limited to several hundred micrometers because of multiple scattering. This limitation is similar to other imaging modalities. Thus, axial scanning through biological tissue beyond the imaging depth still presents a challenge to OBM configuration.

In this study, we demonstrated label-free microendoscopy capable of *in vivo* deep-depth imaging of biological tissue using a thin GRIN lens as a needle-type imaging probe. We mounted the GRIN lens within a medical-grade stainless steel sleeve and attached its rear end to a flexible fiber bundle for further image delivery. We acquired multiple depth images by penetrating the soft tissue with the imaging probe while leaving the OBM configuration-based illumination channels outside. Since the outer diameter of the stainless-steel sleeve was 700 μm , the insertion of the imaging probe into the tissue caused minimum damage. We removed the highly pixelated image artifact due to the discrete nature of the fiber bundle by applying a low-pass filter to the spatial frequency domain. By employing a GRIN lens with a magnification such that the diffraction-limited spot at the sample plane is delivered to the fiber bundle as a point slightly larger than the core spacing, even after the low-pass filtering, the imaging NA of the GRIN lens is not much reduced. Thus, the observed resolution was preserved during being relayed by the fiber bundle remaining close to its diffraction limit. At a specific penetration depth of the imaging probe, we found that the detectable signal depends on the lateral distance of the illumination channels from the imaging probe. We systematically investigated this point through a characterization experiment. We captured two consecutive images by using two different illuminations, one from the left and the other from the right side, so we could acquire an enhanced phase-gradient image. Then, we processed the two raw images to emphasize the object's gradient information. We validated the system performance by experimenting with a tissue phantom. Then we verified the system's feasibility by demonstrating both *ex vivo* and *in vivo* imaging of the microvasculature of mouse brains.

2. Materials and methods

2.1. Experimental system

The schematic of our microendoscope system is depicted in Fig. 1. Two LEDs (S1 and S2, M625L4, Thorlabs) with a wavelength (λ) of 625 nm are used to generate illuminations, where the diverging LED beams are focused onto multimode optical fibers (F1 and F2; M59L01, Thorlabs) for the illumination by aspheric lenses (L1 and L2; $f = 35$ mm). The core diameter and the length of the illumination fibers are 1 mm and 1 m, respectively, and the NA is 0.5, which corresponds to an illumination angle of 30 degrees at the sample surface. The illumination fiber tips are placed at an appropriate distance (d) depending on the depth of probe (h) as shown in the inset in Fig. 1. To precisely adjust the distance d , a fiber holder was fabricated by a 3-D printer, where multiple holes for the illumination fibers were printed every 2 mm spacing. For the needle-type imaging probe, a GRIN-doublet lens (NEM-050-06-08-520-DS, GRINTECH) with a 500 μm

diameter and 3.98 mm length is mounted in a medical-grade stainless steel sleeve with a diameter of 700 μm and a length of 3.98 mm. The working distance and the magnification of the GRIN lens are 60 μm and $2.8\times$ in water, respectively. At the rear end of the GRIN lens, a 1 m-long fiber bundle (FIGH-10-350S, Fujikura) is attached to deliver the acquired image further to a camera (FL3-U3 13Y3M, Point Grey). The fiber bundle has 10,000 cores having a size of 1.7 μm and a fiber diameter of 350 μm . The taken image is relayed to the camera through a beam expander (BE) consisting of a $10\times$ objective lens (OL; Olympus, NA 0.25) and a tube lens (TL; $f=200$ mm, Thorlabs) with a magnification of about $11\times$. Thus, the overall magnification of the microendoscopic system is approximately $31\times$.

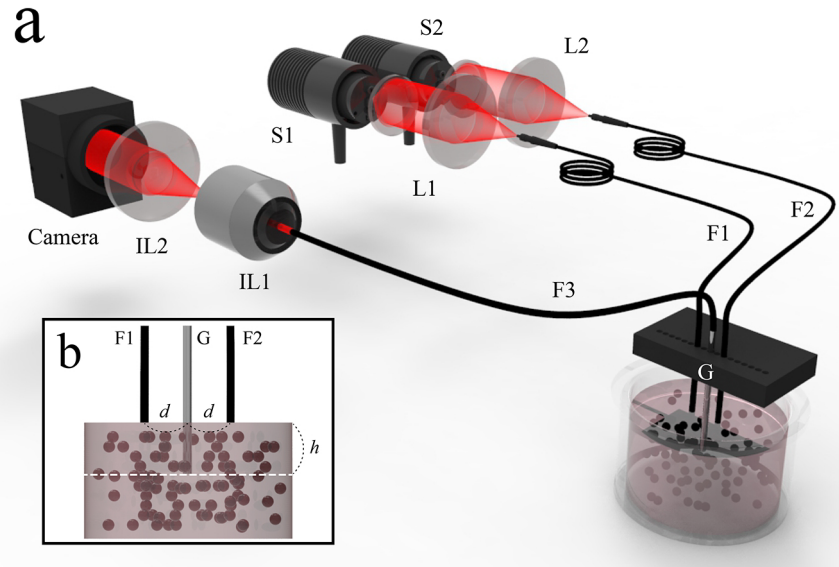


Fig. 1. Experimental schematic for the needle-type microendoscopy. (a) Light from two LEDs (S1, S2) are delivered to the sample surface through multimode optical fibers (F1, F2). The images acquired by the imaging probe are delivered by the fiber bundle (F3) and further relayed to the camera through the beam expander composed of the objective lens (IL1) and the tube lens (IL2). L1 and L2: aspheric focus lens, G: GRIN lens. (b) Zoomed view of the imaging site. d : distance between the imaging probe and illumination fibers, h : penetration depth of the imaging probe.

To acquire a single phase-gradient image, two images are taken with the illuminations, one at a time. The camera exposure for each image is set as 25 ms and the resting period between the two captures is also set as 25 ms. Thus, the total acquisition time during the whole cycle for one phase-gradient image is 100 ms.

2.2. Image processing

To acquire a phase-gradient image, we consecutively captured two different images from the illumination fibers positioned on either side of the imaging probe, one at the left and the other at the right. For the description of the image processing, we used the acquired images of a glass bead embedded in an agarose gel (See Results Sec. 3.3 for more details). The raw images that we obtained are highly pixelated because of the discrete distribution of the cores as shown in Fig. 2(a) for the left channel, and Fig. 2(b) for the right channel. In the Fourier domain, the pixelation comes up with a ring pattern, as shown in the inset in Fig. 2(a). The radius of the ring corresponds to the size of the cores. Its angular spreading (a uniform ring shape) shows the

randomness of the core distribution. To eliminate the pixelation artifact in the spatial domain, we applied a low-pass filter to the Fourier domain and thus removed the ring-shaped angular frequency that the regular structure of the core distribution in the fiber bundle had caused [16,30]. The low-pass filter is constructed by an equation;

$$C(v_x, v_y) = \begin{cases} 1, & v_x^2 + v_y^2 \leq \alpha^2 \\ 0, & v_x^2 + v_y^2 > \alpha^2 \end{cases} \quad (1)$$

where $C(v_x, v_y)$ is a circle-shaped logical function, v_x, v_y are the transverse components of signal strength the spatial frequency $v = \sqrt{v_x^2 + v_y^2} = 2\pi/\lambda$ (λ wavelength of the light), and α is a constant slightly smaller than the radius of the ring-shaped angular frequency. After applying the logical function, the ring-shaped high-frequency noise is removed, as shown in the inset in Fig. 2(c). Since a single core corresponds to a single point in the fiber bundle image, the bandwidth for the spatial frequency is limited by the radius of the ring, and no further information exists in the outer area. Thus, using the low-pass filter neither causes an information loss nor compromises the resolution significantly. The filtered images (I_L' and I_R') are obtained by applying the low-pass filter as follows;

$$I_L'(x, y) = IF\{\tilde{I}_L(v_x, v_y) \times C(v_x, v_y)\}, \quad (2)$$

$$I_R'(x, y) = IF\{\tilde{I}_R(v_x, v_y) \times C(v_x, v_y)\}, \quad (3)$$

where I_L' and I_R' are the filtered images with left and the right illumination, IF is inverse Fourier transform, and \tilde{I}_L and \tilde{I}_R are the Fourier transform of the raw images with the pixelation artifact. The I_L' and I_R' are normalized to the same level of background intensity for the signal strength matches as presented in Figs. 2(c) and 2(d). Even after removing the pixelation, the object structure is still very vague because of the low contrast of the sample. Then the phase-gradient image is produced by subtraction of one image from the other, and the result is shown in Fig. 2(e). The gradient information is now strongly enhanced, particularly along the edge of the sample. Thus, the object feature is considerably emphasized.

2.3. Image resolution

Using a fiber bundle for imaging, the core spacing becomes a primary limiting factor for the imaging resolution. In our case, the average core spacing is 2 μm thus the resolution is no more than that. To minimize this constraint and to achieve microscopic resolution better than the core spacing, we employed a GRIN lens with proper specifications. The GRIN lens has an NA of 0.5, which results in a diffraction-limited spot size of 763 nm at the front focal plane. The diffraction-limited spot is delivered to the rear surface of the GRIN lens, where the fiber bundle is attached, with a magnification of 2.8 \times . Thus, it becomes 2.14 μm at the distal facet of the fiber bundle. This is slightly larger than the core spacing. As a consequence, the optical resolution of the GRIN lens can be almost preserved when the information is relayed by the fiber bundle. Since the diameter of the low-pass filter, which is applied to the Fourier domain of the image (in Sec. 2.2), is determined such that its cutoff size at the bundle surface falls between the 2 μm and 2.14 μm . Thus, the pixelated architecture of the fiber bundle is significantly suppressed but the optical resolution set by the GRIN lens is almost preserved after applying the low-pass filter. Due to the 2.8 \times magnification, the actual achievable resolution at the sample plane is expected as 763 nm at the best.

We also investigated the optical resolution experimentally and verified the above expectation (see Fig. 4 in Sec. 3.2).

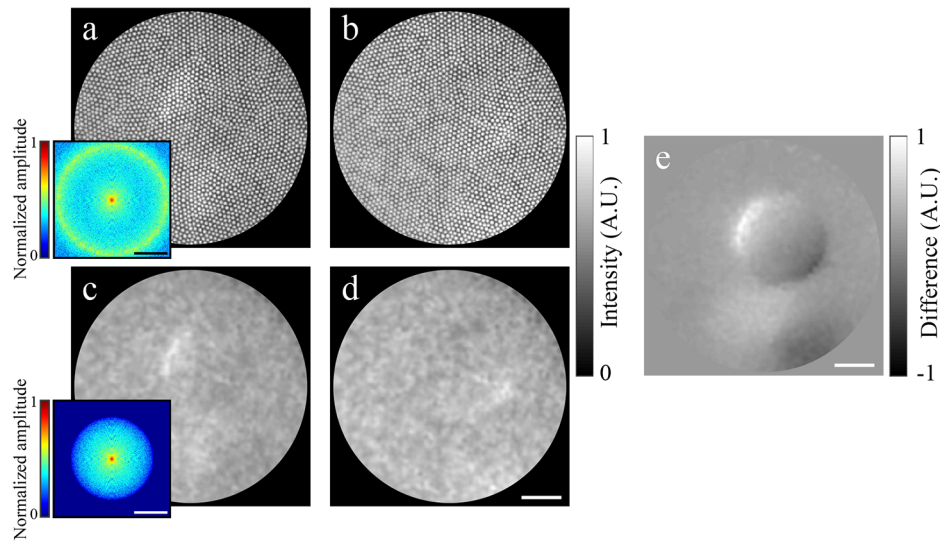


Fig. 2. Image processing for the phase-gradient image of a glass bead embedded in an agarose gel. The (a) and (b) are raw images acquired at the illumination by the left and right channels, and the inset presents the corresponding angular spectrum of the image in (a). The (c) and (d) are processed images after having applied the low-pass filter to (a) and (b), and the inset shows the corresponding angular spectrum of the image in (c). (e) The final phase-gradient image of the bead. Scale bars: $10\ \mu\text{m}$ for (d) and (e), and $3.1\ \mu\text{m}^{-1}$ for the insets. All the images are scaled in the sample plane. Color bars: arbitrary intensity unit.

2.4. Preparation of the mouse brain

All animal experiments in this study were approved by the Korea University Institutional Animal Care and Use Committee (KUIACUC-20150520-1) and were performed in accordance with the relevant guidelines and regulations. We anesthetized the mice with an intraperitoneal injection of a urethane-xylazine mixture of 0.3 mL, 1.2 g/kg urethane, and 20 mg/kg of xylazine. In the case of *ex vivo*, we fixed the brains with a typical perfusion method of 4% paraformaldehyde (PFA) and extracted them. Thereafter, we placed the whole brains in 4% PFA at $4\ ^\circ\text{C}$ overnight. For the *in vivo* brain experiment, we placed the anesthetized mouse on the stage and then restrained it. We then made an incision in the head skin without shaving the fur, and we made a small hole in the skull for the insertion of the probe [31].

3. Results

3.1. Illumination distance for depth imaging

To determine the optimal illumination distance d for a certain imaging depth h , we investigated how d affects the phase contrast and the signal strength of the imaging. For the phase contrast measurement, we prepared a test sample with polystyrene (PS) beads ($23.3\ \mu\text{m}$ diameter, 2.5% w/v, Spherotech) randomly embedded in a 2% agarose gel with 1:1 dilution ratio. The mixture was loaded in a petri-dish with 35 mm diameter. The imaging probe was inserted into the sample and images of PS beads were taken. We kept h once the best focus of a certain PS bead was found during the insertion of the probe and varied d as 2, 4, 6, and 8 mm for the fair comparison of the phase contrasts. One of the typical phase-gradient images of the PS bead and its section profile are shown in the insets in Fig. 3(a). From this section profile, the imaging contrast was measured

as $I_{\max} - I_{\min} / I_{\max} + I_{\min}$. We repeated the measurements at 15 different within the depths up to about 8 mm. The results are presented in Fig. 3(a).

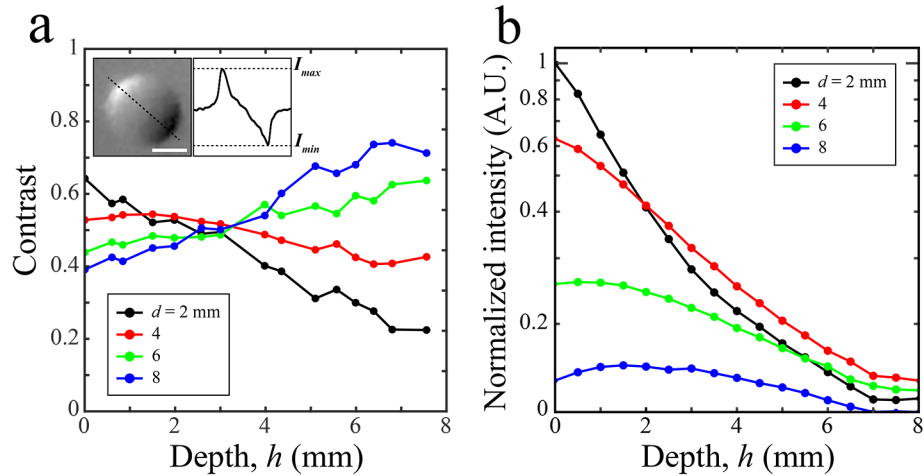


Fig. 3. Phase-gradient contrast and detectable signal strength for various illumination distances (d) and imaging depths (h). (a) The cases of $d = 2, 4, 6$, and 8 mm were represented by black, red, green, and blue in that order. The phase-gradient was obtained from image of PS beads in an agarose gel at 15 different h from 0 to 8 mm. For each of h , we varied d as 2, 4, 6, and 8 mm. The insets showed a representative phase-gradient image of a PS bead and its line profile. Scale bar is 10 μm . (b). The attained signal strength (light intensity) measured at various h and 4 different d . The returning light intensity was measured at every 500 μm depth in a milk solution. During the probe insertion, the illumination fibers were kept touching the surface of the milk solution.

With $d = 2$ mm (black), the contrast was decreased with the increase of h . With $d = 4$ mm (red), it was kept at a similar level up to about $h = 3$ mm and then decreased slowly in a deeper region. Although it was smaller than that with $d = 2$ mm around the sample surface, it became larger after about $h = 1.5$ mm. With $d = 6$ and 8 mm, the contrasts showed lower values than that with $d = 4$ mm near the sample surface, but those kept increasing in general in the whole depth range and eventually became larger than those of others in deeper than $h = 3$ mm. Passing through 3 ~ 4 mm depth, the case of $d = 8$ mm showed the highest contrast. From this observation, we found that when the imaging probe is placed near the surface $h = 0$ to 2 mm, the shorter d causes the higher contrast while for the region deeper than $h = 4$ mm the larger d generates the higher imaging contrast. Around from $h = 2$ to 3 mm, the image contrast does not show any significant difference regardless of the illumination distance.

For the signal strength (intensity) measurements, a milk solution was used as a test medium. We placed the GRIN lens probe and the illumination fibers near the surface of the milk solution, and measured the intensity of the returning light as we changed the insertion depth of the probe from $h = 0$ to 8 mm, with a step size of 500 μm . We repeated the same measurements every 2 mm, at different positions of the illumination channels, from $d = 2$ mm to 8 mm. Since the scattering coefficient ($\mu_s \sim 500 \text{ cm}^{-1}$) of milk solution is similar to that of skin tissues, we can estimate the optimal illumination distance for depth imaging of tissues by this experiment. At the smallest distance, $d = 2$ mm, the observed light intensity monotonically decays from the surface along the depth direction ($h = 0 \sim 8$ mm). For imaging depths shallower than $h = 2$ mm, the illumination of $d = 2$ mm shows the detection efficiency better than at any other distance used in the experiment. But at an imaging depth greater than $h = 2$ mm, the detection intensity becomes smaller than that of $d = 4$ mm. At $d = 4$ mm, the detected light strength is not as good as

that with $d = 2$ mm in the shallow region. But this is reversed when we place the probe deeper than $h = 2$ mm. At $d = 6$ mm and 8 mm, the detected light intensity is always smaller than in those cases where $d = 2$ mm and 4 mm.

Since the phase contrast is comparable to the illumination distance d within the depth range h of 2 ~ 3 mm, which is the target imaging depth for our study, the signal strength can be considered as the metric for the determination of the optimum imaging condition. As shown in Fig. 3(b), in that depth range, $d = 4$ mm generates the highest detection signal. Considering both the experimental results, we decided the optimal imaging parameter for the illumination distance as $d = 4$ mm in our study.

3.2. Validation of the imaging system

To validate the imaging capability of our microendoscope system, we performed simple imaging of test objects. For the experiment, we prepared a scattering phantom tissue with a mixture of PS beads and PDMS. Before its solidification, a USAF target was placed in the middle of the phantom, 2 mm from the surface, and 10 mm from the bottom. After being solidified, the sample included the target between the two phantom layers of which thicknesses were enough for the OBM configuration. The scattering mean free path of the tissue phantom was measured as about 110 μm . The illumination fibers were placed at $d = 4$ mm distance from the probe for optimal signal detection. We acquired two images consecutively and then processed the two images to obtain the phase-gradient images. In Fig. 4(a), we present the image of elements 3 through 6 in group 7 of the USAF target. Although the USAF target is not a phase object, the structures were well visualized with no significant deformation. The field of view was a circular area with 114 μm in diameter.

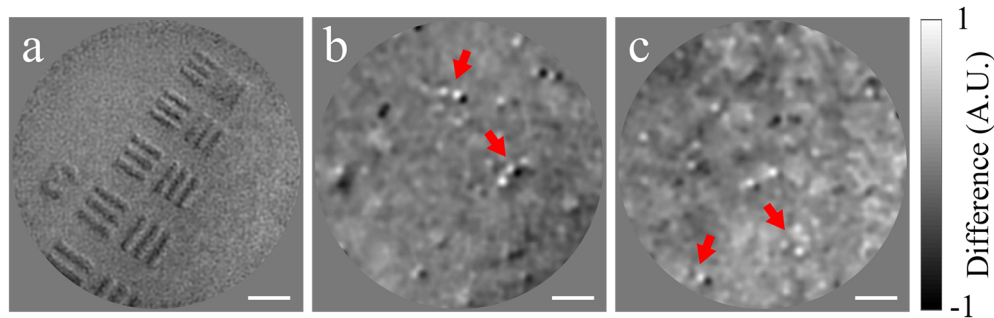


Fig. 4. (a) Processed image of a 1951 USAF target in an agarose gel. Scale bar: 15 μm . (b), (c) Phase-gradient images of (b) 1 μm PS beads and (c) 750 nm PS beads in agarose gels. Scale bars in (b) and (c): 5 μm .

Next, to investigate the actual achievable resolution of our microendoscope we made two agarose gels, one including 1 μm PS beads and the other 750 nm PS beads, with similar preparation procedures described in Sec. 3.1. The phase-gradient images for both the samples were obtained around at 2 mm depth and a 4 mm illumination distance. The results are presented in Figs. 4(b) and 4(c). The 1 μm PS beads are well resolved as denoted by the arrows in Fig. 4(b). The 750 nm beads are also resolved as presented in Fig. 4(c) but the distinction is not as good as that in Fig. 4(b). This confirms that the achieved resolution is near 750 nm, close to the ideal resolution without significant degradation. By employing the GRIN lens with the proper NA and magnification its diffraction-limited spot size is matched well with the core spacing of the fiber bundle. Due to this configuration, the optical resolution achieved by the GRIN lens can be almost preserved when images are relayed by the fiber bundle.

3.3. Depth imaging

The main advantage of our microendoscope system is its capability of depth imaging through a sample in a minimally invasive manner. To confirm this point, we demonstrated depth imaging of glass beads embedded in a slab of agarose gel (~ 10 mm thickness). In the gel, we randomly distributed glass beads of various diameters ranging from 10 to 50 μm , which were fixed in their positions. The insertion depth of the imaging probe into the gel varied from 0 mm up to 3 mm. During the depth scanning, we found two beads that were located at slightly different depths as schematically presented in Fig. 5(a). At 1 mm depth from the top surface of the gel, the upper bead appeared as denoted with the red dotted circle in Fig. 5(b). Following that, we measured the relative scanning depth of the imaging probe from this position. We further moved the probe in a downward direction by 100 μm in total. During the scanning, we acquired images at every 5 μm (see Visualization 1). Representative images taken are shown in Figs. 5(b) ~ 5(f), at 0 μm , 25 μm , 50 μm , 75 μm , and 100 μm , in that order. Going deeper, the upper bead, which appears very blurry in Fig. 5(b), looks fairly sharp in Fig. 5(c). The upper bead again can be seen indistinctly, and the lower bead (whose location is denoted by the blue dotted circle) starts to be resolved in Fig. 5(d). Going further, in Fig. 5(f), the upper bead is significantly blurred and the lower

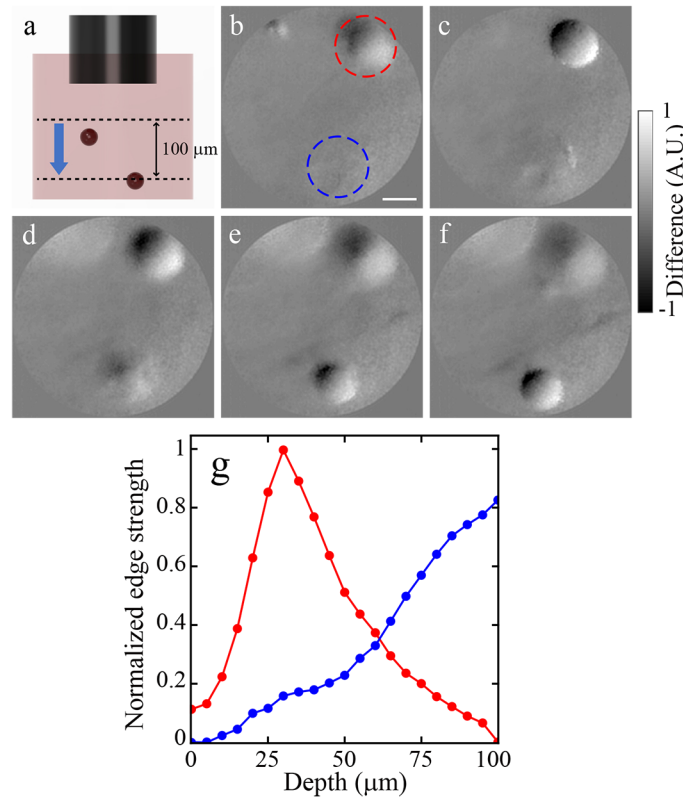


Fig. 5. Depth imaging of glass beads by the invasion of the probe through a thick agarose gel. (a) Schematic of the imaging configuration. The initial invasion depth of the probe is 1 mm from the surface of the gel. (b) - (f) Phase-gradient images of the beads acquired at different depths. (b) 0 μm , (c) 25 μm , (d) 50 μm , (e) 75 μm and (f) 100 μm , where the depth is relatively presented from the initial invasion depth of the probe (Visualization 1). (g) The normalized edge strength of the two beads denoted by the circles with the same colors in (b). Scale bar: 20 μm .

one is near the focus as shown in [Visualization 1](#). To more systematically investigate the ability of the imaging system to perform depth profiling, we applied the edge strength analysis to the acquired images. The edge strength is the sum of all the differential values over the imaging region of interest and is often used as a metric for the assessment of imaging sharpness [32,33]. Figure 5(g) shows the measured edge strength for both the beads normalized to the highest value. As shown in the plot in red, we can find the best focus of the upper bead at 30 μm from its full width at half maximum (FWHM). This is quite consistent with the lateral dimension of the same bead measured in Fig. 5. For the lower bead, as shown in the plot in blue, the location of the best focus is thought to be near 100 μm .

3.4. *Ex vivo* and *in vivo* brain imaging

We investigated the microendoscope system's capability to perform imaging of biological structures. To confirm the feasibility of using it, we performed both *ex vivo* and *in vivo* imaging of mouse brains. We anesthetized the mice by intraperitoneal injection of a urethane-xylazine mixture of 0.3 mL (see Materials and Method Sec. 2.4 for more details). In the case of the *ex vivo* imaging, we fixed the mouse brain by a normal perfusion method, using 4% paraformaldehyde and then extracted it. We treated the fixed brain by using a post-fixation procedure and then placed it on the stage. For the *in vivo* brain imaging, we placed the anesthetized mouse on the stage and fastened it. Then we incised the head skin of the mouse without first shaving the fur. Then we made a small hole in the skull for insertion of the imaging probe.

In the *ex vivo* imaging, we inserted the imaging probe into the brain at 2 mm from the brain surface. At this depth, we could see an about 20 μm diameter microvessel structure as shown in Fig. 6(a). Moving 20 μm deeper, we found that a small, approximately 5 μm branch had split

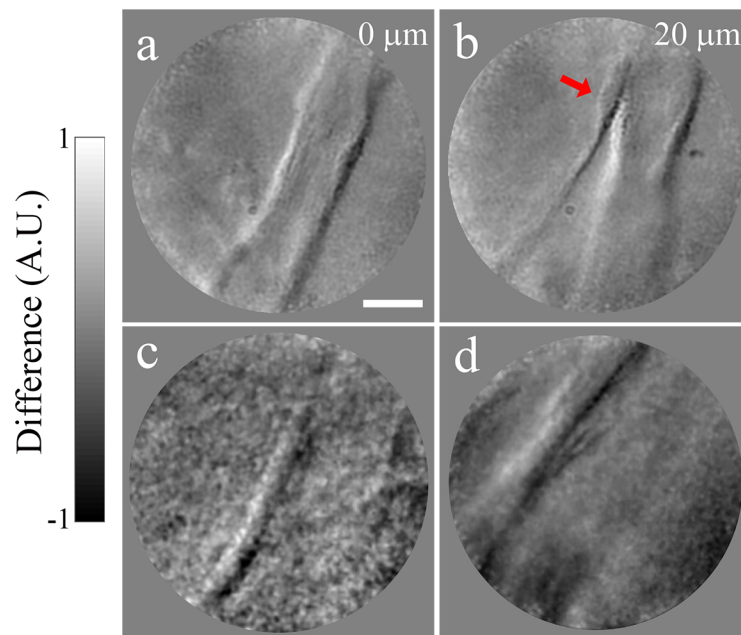


Fig. 6. *Ex vivo* and *in vivo* imaging of mouse brains. (a) *Ex vivo* image of a blood vessel acquired at 0 μm . (b) The same as (a) but taken at 20 μm . A small branch splitting from the main vessel is denoted with the red arrow. The depth was relatively measured from the initial invasion depth of the probe, 2 mm from the surface of the brain. (c) and (d) *In vivo* images of blood vessels acquired with two different brain samples. Scale bar: 20 μm .

from the mainstream as the red arrow indicates in Fig. 6(b). Even in the *in vivo* imaging, it was possible to observe some structures at different depths that appeared to be microvasculature. Figures 6(c) and 6(d) show microvessels that were approximately 15 μm , that we had acquired from two different mice.

4. Discussion

In the field of biomedical imaging, there is a continuing interest in being able to reach deeper into living tissue so as to observe more details. However, this primary concern has been limited by the multiple scattering inevitable in biological tissue. Recently, plenty of technical innovations have been made that focus on enhancing the resolution and improving the penetration depth of optical imaging modalities for both *ex vivo* and *in vivo* conditions [34]. The mainstream has been based on cutting-edge wavefront sensing and controlling techniques, so-called AO, to suppress the effect of multiple scattering [14,18,19]. The illumination wavefront is controlled to generate a sharp focus inside tissue and the spot is steered toward acquiring the structural images by fluorescence imaging [35,36]. The optical properties of the returning wave were acquired as a reflection matrix and analyzed to generate the scatter-free images in reflectance imaging [16,37,38]. The imaging depth was enhanced by the combination of the acoustic modulation with optical imaging [19,39]. Although these techniques allow high-resolution imaging of intact tissue to deeper regions than conventional methods permit, it is still impossible to completely overcome the inherent limitation set by the multiple scattering in biological tissue. Moreover, the strict requirement of sophisticated imaging conditions, the unsustainability of the complex optical configurations, and the computational load for complicated image processing make it difficult to use those techniques for practical applications. Such highly advanced techniques in actual practices are far from being achieved.

Our system, in contrast, has certain advantages regarding the issues raised above. First, this imaging technique can reach even deeper into biological tissues than can the conventional methods. By inserting this thin imaging probe, we can achieve a much greater depths than can the conventional technique, which only reaches several hundred microns. The technique we present reaches a depth that is order-of-magnitude greater, and achieves that with minimal invasion. In non-invasive approaches, imaging depth limitations and multiple scattering during light return are the main causes of the information loss about the object. On the other hand, our method has no such restrictions caused by direct access to target objects, but the main barrier to imaging depth is in the diffusion range reachable by illumination. Although the imaging probe is inserted minimally into the tissue, the illumination channels still stay at the surface. Thus, the achievable imaging depth is limited to the maximum diffusion length of light in our case.

Second, our microendoscope system is very suitable for imaging because of its simple optical configuration. Since the system employs a direct penetration approach, it does not require the same complex optical elements for reducing the effect of multiple scattering as do the AO-based methods. In our system, the key optical elements are simply the GRIN lens probe capturing the object information and the fiber bundle delivering the acquired images. And an uncomplicated process generates the final image. The necessity of less sophisticated optical components, as well as the undemanding computational burden, makes our method more robust than the other methods in use.

In addition to this, although our system employs a reflection configuration, it is light transmission through the sample that forms the image contrast. This is critical for label-free imaging, especially for most *in vivo* situations where acquiring transmission images is unavailable. Since most biological samples have very low reflectivity in visible light, the label-free imaging for tissue based on its reflectance inevitably shows weak contrast and poor signal-to-noise ratio. But, in our microendoscopy method, the illumination light introduced at the superficial plane of the tissue can reach the backside of the target depth via diffusion. This then transmits through the

object, at which point the absorbed light generates a fairly good imaging contrast, compared to the reflectance approach. Thus, our method can provide imaging with superior contrast even in the *in vivo* situation.

Unlike the conventional OBM, where both the illumination and the detection channels were placed outside, in our method, we place a thin imaging probe into the tissue to reach the depth of interest. By leaving the illumination channels outside, we achieve the depth imaging in a minimally invasive manner. As the detected signal depends on the distance of the illumination spots from the detection port, the optical imaging condition can be found, depending on the imaging depth.

Although a very thin imaging probe is used, it inevitably causes a certain amount of damage to the tissue when it is inserted. Thus, it is very difficult to re-observe the same structure at the same site although a living tissue can recover the insertion damage. Even with this drawback, the advantage of our method is very clear. Since the imaging is less affected by the light scattering, our method can access even deeper regions where the non-invasive techniques have not been reached yet.

In summary, we demonstrated a microendoscopy technique capable of *in vivo* imaging up to a depth of several millimeters into biological tissue employing a thin GRIN lens mounted in a medical-grade stainless steel sleeve as an imaging probe for tissue invasion. By penetrating the imaging probe through a sample, the target depth is able to be directly investigated. We obtained the images with an OBM illumination configuration. The images that the probe captured were delivered to the detector through a flexible fiber bundle, and we removed the pixelation artifact by applying a low-pass filter in the Fourier domain. After the image processing, we achieved a resolution close to the diffraction limit of the GRIN lens. In the test experiments performed in a milk solution, we found that the observed signal depends not only on the penetration depth of the imaging probe but also on the location of the illumination channels. By considering signal dependence, we determined the optimal separation of the illumination channels from the imaging probe, especially for target depths beyond 2 mm. We confirmed the capability of depth imaging by observing glass beads in a tissue phantom. We used the microendoscope for *ex vivo* and *in vivo* imaging of mouse brains and visualized microvasculature. Since our microendoscope features a simple optical configuration, uncomplicated image processing, and ease of use, it has a great deal of potential for being widely used as a tool for tissue biopsy and microsurgical guidance.

Funding

Korea University Grant (Korea University Grant); National Research Foundation of Korea (2017R1A6A3A11031083, 2019H1A2A1076334, 2019R1A2C4004804); National Eye Institute (R01EY030569); Institute of Information and Communications Technology Planning and Evaluation (IITP; MSIT) (2020-0-00997).

Disclosures

The authors declare no conflicts of interest.

References

1. A. Méndez, "Optics in Medicine," in *Optics in Our Time* (Springer, 2016), pp. 299–333.
2. F. Xia, C. Wu, D. Sinefeld, B. Li, Y. Qin, and C. Xu, "In vivo label-free confocal imaging of the deep mouse brain with long-wavelength illumination," *Biomed. Opt. Express* **9**(12), 6545–6555 (2018).
3. W. Denk, J. H. Strickler, and W. W. Webb, "Two-photon laser scanning fluorescence microscopy," *Science* **248**(4951), 73–76 (1990).
4. J. C. Jung, A. D. Mehta, E. Aksay, R. Stepnoski, and M. J. Schnitzer, "In vivo mammalian brain imaging using one- and two-photon fluorescence microendoscopy," *J. Neurophysiol.* **92**(5), 3121–3133 (2004).
5. D. A. Dombeck, C. D. Harvey, L. Tian, L. L. Looger, and D. W. Tank, "Functional imaging of hippocampal place cells at cellular resolution during virtual navigation," *Nat. Neurosci.* **13**(11), 1433–1440 (2010).

6. P. Theer, M. T. Hasan, and W. Denk, "Two-photon imaging to a depth of 1000 μm in living brains by use of a $\text{Ti:Al}_2\text{O}_3$ regenerative amplifier," *Opt. Lett.* **28**(12), 1022–1024 (2003).
7. Y. G. Kang, H. Jang, T. D. Yang, J. Notbohm, Y. Choi, Y. Park, and B.-M. Kim, "Quantification of focal adhesion dynamics of cell movement based on cell-induced collagen matrix deformation using second-harmonic generation microscopy," *J. Biomed. Opt.* **23**(6), 065001 (2018).
8. S. W. Hell, K. Bahlmann, M. Schrader, A. Soini, H. M. Malak, I. Gryczynski, and J. R. Lakowicz, "Three-photon excitation in fluorescence microscopy," *J. Biomed. Opt.* **1**(1), 71–75 (1996).
9. D. L. Wokosin, V. E. Centonze, S. Crittenden, and J. White, "Three-photon excitation fluorescence imaging of biological specimens using an all-solid-state laser," *Bioimaging* **4**(3), 208–214 (1996).
10. N. G. Horton, K. Wang, D. Kobat, C. G. Clark, F. W. Wise, C. B. Schaffer, and C. Xu, "In vivo three-photon microscopy of subcortical structures within an intact mouse brain," *Nat. Photonics* **7**(3), 205–209 (2013).
11. J. G. Fujimoto, M. E. Brezinski, G. J. Tearney, S. A. Boppart, B. Bouma, M. R. Hee, J. F. Southern, and E. A. Swanson, "Optical biopsy and imaging using optical coherence tomography," *Nat. Med.* **1**(9), 970–972 (1995).
12. J. Lee, W. Wu, and D. A. Boas, "Early capillary flux homogenization in response to neural activation," *J. Cereb. Blood Flow Metab.* **36**(2), 375–380 (2016).
13. M. G. Hyeon, H.-J. Kim, B.-M. Kim, and T. J. Eom, "Spectral domain optical coherence tomography with balanced detection using single line-scan camera and optical delay line," *Opt. Express* **23**(18), 23079–23091 (2015).
14. S. Kang, S. Jeong, W. Choi, H. Ko, T. D. Yang, J. H. Joo, J.-S. Lee, Y.-S. Lim, Q.-H. Park, and W. Choi, "Imaging deep within a scattering medium using collective accumulation of single-scattered waves," *Nat. Photonics* **9**(4), 253–258 (2015).
15. Y. Choi, T. D. Yang, C. Fang-Yen, P. Kang, K. J. Lee, R. R. Dasari, M. S. Feld, and W. Choi, "Overcoming the diffraction limit using multiple light scattering in a highly disordered medium," *Phys. Rev. Lett.* **107**(2), 023902 (2011).
16. Y. Choi, C. Yoon, M. Kim, T. D. Yang, C. Fang-Yen, R. R. Dasari, K. J. Lee, and W. Choi, "Scanner-free and wide-field endoscopic imaging by using a single multimode optical fiber," *Phys. Rev. Lett.* **109**(20), 203901 (2012).
17. Y. Choi, T. R. Hillman, W. Choi, N. Lue, R. R. Dasari, P. T. So, W. Choi, and Z. Yaqoob, "Measurement of the time-resolved reflection matrix for enhancing light energy delivery into a scattering medium," *Phys. Rev. Lett.* **111**(24), 243901 (2013).
18. S. Kang, P. Kang, S. Jeong, Y. Kwon, T. D. Yang, J. H. Hong, M. Kim, K. D. Song, J. H. Park, and J. H. Lee, "High-resolution adaptive optical imaging within thick scattering media using closed-loop accumulation of single scattering," *Nat. Commun.* **8**(1), 1–10 (2017).
19. M. Kim, Y. Jo, J. H. Hong, S. Kim, S. Yoon, K.-D. Song, S. Kang, B. Lee, G. H. Kim, and H.-C. Park, "Label-free neuroimaging in vivo using synchronous angular scanning microscopy with single-scattering accumulation algorithm," *Nat. Commun.* **10**(1), 1–9 (2019).
20. T. N. Ford, K. K. Chu, and J. Mertz, "Phase-gradient microscopy in thick tissue with oblique back-illumination," *Nat. Methods* **9**(12), 1195–1197 (2012).
21. T. N. Ford and J. Mertz, "Video-rate imaging of microcirculation with single-exposure oblique back-illumination microscopy," *J. Biomed. Opt.* **18**(6), 066007 (2013).
22. J. D. Giese, T. N. Ford, and J. Mertz, "Fast volumetric phase-gradient imaging in thick samples," *Opt. Express* **22**(1), 1152–1162 (2014).
23. J. Mertz, A. Gasecka, A. Daradich, I. Davison, and D. Coté, "Phase-gradient contrast in thick tissue with a scanning microscope," *Biomed. Opt. Express* **5**(2), 407–416 (2014).
24. J. Li, T. G. Bifano, and J. Mertz, "Widefield fluorescence microscopy with sensor-based conjugate adaptive optics using oblique back illumination," *J. Biomed. Opt.* **21**(12), 121504 (2016).
25. T. D. Weber and J. Mertz, "Non-mydratic chorioretinal imaging in a transmission geometry and application to retinal oximetry," *Biomed. Opt. Express* **9**(8), 3867–3882 (2018).
26. H. P. Paudel, C. Alt, J. Runnels, and C. P. Lin, "Pupil plane differential detection microscopy," *Opt. Lett.* **43**(18), 4410–4412 (2018).
27. P. Ledwig, M. Sghayyer, J. Kurtzberg, and F. E. Robles, "Dual-wavelength oblique back-illumination microscopy for the non-invasive imaging and quantification of blood in collection and storage bags," *Biomed. Opt. Express* **9**(6), 2743–2754 (2018).
28. G. N. McKay, N. Mohan, and N. J. Durr, "Imaging human blood cells in vivo with oblique back-illumination capillaroscopy," *Biomed. Opt. Express* **11**(5), 2373–2382 (2020).
29. P. Ledwig and F. E. Robles, "Epi-mode tomographic quantitative phase imaging in thick scattering samples," *Biomed. Opt. Express* **10**(7), 3605–3621 (2019).
30. D. Kim, J. Moon, M. Kim, T. D. Yang, J. Kim, E. Chung, and W. Choi, "Toward a miniature endomicroscope: pixelation-free and diffraction-limited imaging through a fiber bundle," *Opt. Lett.* **39**(7), 1921–1924 (2014).
31. J. H. Kim, M. J. Jang, J. Choi, E. Lee, K. D. Song, J. Cho, K.-T. Kim, H.-J. Cha, and W. Sun, "Optimizing tissue-clearing conditions based on analysis of the critical factors affecting tissue-clearing procedures," *Sci. Rep.* **8**(1), 1–11 (2018).
32. P. Langehanenberg, B. Kemper, D. Dirksen, and G. Von Bally, "Autofocusing in digital holographic phase contrast microscopy on pure phase objects for live cell imaging," *Appl. Opt.* **47**(19), D176–D182 (2008).

33. E. S. Fonseca, P. T. Fiadeiro, M. Pereira, and A. Pinheiro, "Comparative analysis of autofocus functions in digital in-line phase-shifting holography," *Appl. Opt.* **55**(27), 7663–7674 (2016).
34. S. Yoon, M. Kim, M. Jang, Y. Choi, W. Choi, S. Kang, and W. Choi, "Deep optical imaging within complex scattering media," *Nat. Rev. Phys.* **2**(3), 141–158 (2020).
35. D. E. Wagner, C. Weinreb, Z. M. Collins, J. A. Briggs, S. G. Megason, and A. M. Klein, "Single-cell mapping of gene expression landscapes and lineage in the zebrafish embryo," *Science* **360**(6392), 981–987 (2018).
36. J. H. Hines, A. M. Ravanelli, R. Schwindt, E. K. Scott, and B. Appel, "Neuronal activity biases axon selection for myelination in vivo," *Nat. Neurosci.* **18**(5), 683–689 (2015).
37. M. G. Hyeon, T. D. Yang, J.-S. Park, K. Park, Y. G. Kang, B.-M. Kim, and Y. Choi, "Reflection phase microscopy by successive accumulation of interferograms," *ACS Photonics* **6**(3), 757–766 (2019).
38. M. Kim, Y. Choi, C. Yoon, W. Choi, J. Kim, Q.-H. Park, and W. Choi, "Maximal energy transport through disordered media with the implementation of transmission eigenchannels," *Nat. Photonics* **6**(9), 581–585 (2012).
39. M. Jang, H. Ko, J. H. Hong, W. K. Lee, J.-S. Lee, and W. Choi, "Deep tissue space-gated microscopy via acousto-optic interaction," *Nat. Commun.* **11**(1), 1–11 (2020).